

AD-A104 377

AIR FORCE GEOPHYSICS LAB HANSCOM AFB MA
AN ASSESSMENT OF DETECTING MESOSCALE RAINFALL FROM MID-LATITUDE--ETC(U)
MAR 81 R F FOURNIER

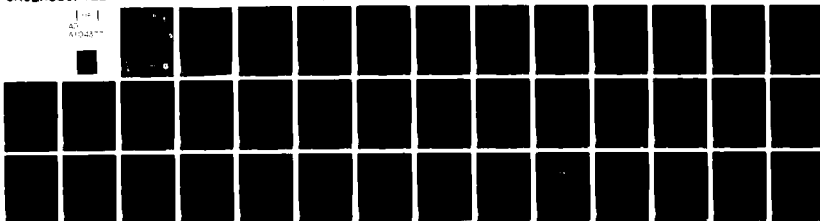
F/G 4/2

UNCLASSIFIED

AFGL-TR-81-0089

NL

1-1
45
AFGL-TR-81-0089



END
DATE
FILED
0-81
DTIC

AD A 104 377

✓ AFGL-TR-81-0089
ENVIRONMENTAL RESEARCH PAPERS, NO. 735

LEVEL

42
B-5



**An Assessment of Detecting Mesoscale Rainfall
From Mid-Latitude Cyclones
Using GOES Imagery Data**

RONALD F. FOURNIER



25 March 1981

Approved for public release; distribution unlimited.

METEOROLOGY DIVISION
AIR FORCE GEOPHYSICS LABORATORY
HANSCOM AFB, MASSACHUSETTS 01731

PROJECT 6670

AIR FORCE SYSTEMS COMMAND, USAF



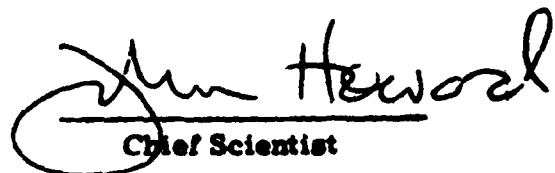
81 9 18 067

3 FILE COPY
B

This report has been reviewed by the ESD Information Office (OI) and is
releasable to the National Technical Information Service (NTIS).

This technical report has been reviewed and
is approved for publication.

FOR THE COMMANDER



John Howard
Chief Scientist

Qualified requestors may obtain additional copies from the
Defense Technical Information Center. All others should apply to the
National Technical Information Service.

12
Unclassified

SECURITY CLASSIFICATION OF THIS PAGE (When Data Entered)

REPORT DOCUMENTATION PAGE		READ INSTRUCTIONS BEFORE COMPLETING FORM
1. REPORT NUMBER AFGL-TR-81-0089	2. GOVT ACCESSION NO. AD-A104 397	3. RECIPIENT'S CATALOG NUMBER
4. TITLE (and subtitle) AN ASSESSMENT OF DETECTING MESOSCALE RAINFALL FROM MID-LATITUDE CYCLONES USING GOES IMAGERY DATA	5. TYPE OF REPORT & PERIOD COVERED Scientific. Interim.	6. PERFORMING ORG. REPORT NUMBER ERP No. 735
7. AUTHOR(s) Ronald F. Fournier	8. CONTRACT OR GRANT NUMBER(s)	
9. PERFORMING ORGANIZATION NAME AND ADDRESS Air Force Geophysics Laboratory (LYU) Hanscom AFB Massachusetts 01731	10. PROGRAM ELEMENT, PROJECT, TASK AREA & WORK UNIT NUMBERS 62101F 111 6670B04	
11. CONTROLLING OFFICE NAME AND ADDRESS Air Force Geophysics Laboratory (LYU) Hanscom AFB Massachusetts 01731	12. REPORT DATE 25 March 1981	13. NUMBER OF PAGES 40
14. MONITORING AGENCY NAME & ADDRESS (if different from Controlling Office)	15. SECURITY CLASS. (of this report) Unclassified	15a. DECLASSIFICATION/DOWNGRADING SCHEDULE
16. DISTRIBUTION STATEMENT (of this Report) Approved for public release; distribution unlimited.	17. DISTRIBUTION STATEMENT (of the abstract entered in Block 20, if different from Report) SEP 1 1981	
18. SUPPLEMENTARY NOTES Research for this report was conducted at the Massachusetts Institute of Technology under sponsorship of the Air Force Systems Command long-term, full-time training program.		
19. KEY WORDS (Continue on reverse side if necessary and identify by block number) Meteorology Satellite threshold Rain gages Weather satellites Weather radar Mesoscale precipitation Satellite imagery Radar threshold Visible sensor Radar echoes Infrared sensor Rainfall mass flux		
20. ABSTRACT (Continue on reverse side if necessary and identify by block number) This study examined the capability of current geostationary satellite sensors in resolving and monitoring important mesoscale rain areas. Shallow mesoscale precipitation patterns were analyzed with radar and recording rain gage data associated with mid-latitude cyclones in New England. These cyclones were characterized by relatively little stratiform cloudiness in the upper troposphere. Radar thresholding was used to determine the spatial and temporal scales of small mesoscale areas (SMSAs), large mesoscale areas		

DD FORM 1 JAN 73 1473

Unclassified

SECURITY CLASSIFICATION OF THIS PAGE (When Data Entered)

Unclassified

SECURITY CLASSIFICATION OF THIS PAGE(When Data Entered)

20. Abstract (Continued)

(LMSAs), and major echoes. Radar rainfall estimates were used to determine the relative amount of rainfall contributed by the mesoscale features. Radar analysis of the three cases showed that the spatial scale of major echoes, LMSAs, and SMSAs were large enough for detection by GOES sensors. Major echoes and the LMSAs contained within them were found to have lifetimes that are long relative to the half-hour interval between GOES transmissions. The duration of some SMSAs and all cells, however, was on the same order as the time interval between GOES transmissions. In addition, radar rainfall estimates showed that the major echoes, LMSAs, and SMSAs were the major contributors to mesoscale rainfall.

Examination of the visible and infrared satellite imagery revealed that the clouds detected in the infrared imagery in the vicinity of major radar echoes were slightly colder than nearby nonprecipitating cloud areas. The visible imagery, however, could not separate raining from nonraining areas. Detailed comparisons between distribution of hourly recording rain gage observations and satellite imagery showed that approximately 80 percent of the rain gage sites that reported measurable rain were within the cold cloud area. However, a relatively small percentage (2 to 48 percent) of the gages located within the colder infrared area actually recorded measurable rain. Detailed analysis of the time change of radar echo areas showed little correspondence. For the cases examined in this study, GOES sensors were not capable of distinguishing the individual mesoscale precipitation areas detected by radar. Therefore, GOES sensors do not appear adequate for developing satellite rainfall estimation techniques to specify shallow mesoscale precipitation.

A

Accession No.	
NTIS	GT & I
DTIC	T-1
Unclassified	
Joint	
By	
Distribution/	
Aviation City Codes	
A, B, C, D, E, F, G, H, I, J, K, L, M, N, O, P, Q, R, S, T, U, V, W, X, Y, Z	
P, Q, R, S, T, U, V, W, X, Y, Z	
P, Q, R, S, T, U, V, W, X, Y, Z	
A	

Unclassified

SECURITY CLASSIFICATION OF THIS PAGE(When Data Entered)

Preface

The author is grateful to the United States Air Force for making possible this study at M.I.T., and to Mr. Donald A. Chisholm, Chief, Mesoscale Forecasting Branch, Meteorology Division, AFGL, for encouraging and supporting it.

He also expresses special appreciation to Dr. Robert Burpee (Visiting Professor of Meteorology), whose guidance during the preparation of this study was invaluable. Also appreciated are the efforts of: Mr. Thomas J. Keegan and Dr. H. Stuart Muench, for many valuable suggestions on the manuscript; John Powers, for drafting the figures; and Karen A. Sullivan, for typing the manuscript.

Contents

1. INTRODUCTION	9
2. MESOSCALE STRUCTURE OF PRECIPITATION WITHIN EXTRATROPICAL CYCLONES	11
3. CASE STUDY OF THREE NEW ENGLAND RAIN EVENTS	14
3.1 Selection of Cases	14
3.2 The Data Bases	14
3.3 Characteristics of the Precipitation	17
4. RESULTS OF RADAR ANALYSES	18
4.1 Characteristics of Mesoscale Features	19
4.2 Rainfall Characteristics of Mesoscale Features	20
5. RESULTS OF SATELLITE DATA ANALYSES	28
5.1 Satellite and Rain Gage Comparisons	28
5.2 Delineation of Rainfall Areas by Thresholding the Satellite Imagery	28
5.3 Satellite Threshold and Rain Gage Comparisons	30
5.4 Satellite and Radar Comparisons	30
6. CONCLUSIONS	34
REFERENCES	39

Illustrations

1. Proposed Areal Extent of Mesoscale Precipitation Areas	12
2. Schematic of Mesoscale Areas	13
3. Echo A Area Summary	21
4. Echo B Area Summary	21
5. Echo C Area Summary	22
6. Echo D Area Summary	22
7. Echo E Area Summary	23
8. Contribution of Major Echo A to Total Estimated Rainfall	25
9. Contribution of Major Echo B to Total Estimated Rainfall and Contribution by Mesoscale Features to Major Echo B	25
10. Contribution of Major Echo C to Total Estimated Rainfall and Contribution by Mesoscale Features to Major Echo C	26
11. Contribution of Major Echo D to Total Estimated Rainfall and Contribution by Mesoscale Features to Major Echo D	26
12. Contribution of Major Echo E to Total Estimated Rainfall and Contribution by Mesoscale Features to Major Echo E	27
13. Typical IR Frequency Distribution for 19 April and 15 May	29
14. The 1800 GMT, 172 IR Digital Count Satellite Threshold Area (dashed line) and the 1758 GMT, 26-dBZ Radar Reflectivity (stippled area) on 19 April 1978	31
15. The 2000 GMT, 175 IR Digital Count Satellite Threshold Area (dashed line) and the 2002 GMT, 26 dBZ Radar Reflectivity Level (stippled area) on 15 May 1978	31
16. The 1902 GMT, 26 dBZ (stippled areas), 30 dBZ (dark areas) Radar Reflectivity Levels and the 1900 GMT Colder IR Areas Associated With Major Echo A (short dashed lines), B (long dashed line) and C for 19 April 1978	36

Tables

1. Dates and Time Periods Used in This Study	14
2. Characteristics of MIT WR66 and WR73 Weather Radars	15
3. Time of Radar Maps for the Three Selected Cases	15
4. Time of Satellite Images Used in the Three Cases	17
5. Frequency of Rainfall Rates for All Stations, for Each Case, and for All Three Cases	18
6. Temporal Summary of the Five Major Echoes Detected by Radar for 19 April and 15 May 1978	19

Tables

7. Temporal Summary of SMSAs and LMSAs Within the Five Major Echoes Detected on 19 April and 15 May 1978	20
8a. Percentage Contribution to Total Mass Flux of Radar Map by the Major Echoes for 19 April 1978	24
8b. Percentage Contribution to Total Mass Flux of Radar Map by the Major Echoes for 15 May 1978	24
9a. Frequency Distribution of Rainfall Rates Inside Optimum IR Threshold Area for 19 April 1978	32
9b. Frequency Distribution of Rainfall Rates Outside Optimum IR Threshold Area for 19 April 1978	32
10a. Frequency Distribution of Rainfall Rates Inside Optimum IR Threshold Area for 15 May 1978	33
10b. Frequency Distribution of Rainfall Rates Outside Optimum IR Threshold Area for 15 May 1978	33
11. Correlation Coefficients of the Time Variation of Both Radar Echo Area and Precipitation Mass Flux to Satellite IR Area for the Major Echoes	35

An Assessment of Detecting Mesoscale Rainfall From Mid-Latitude Cyclones Using GOES Imagery Data

1. INTRODUCTION

For many years there have been near real-time and real-time requirements for specifying rainfall amounts over synoptic scale areas ($>10,000 \text{ km}^2$) more accurately and quickly than with the conventional rain-gage network. A rainfall amount measured by a single rain gage for a large area (1,000 to $10,000 \text{ km}^2$) usually is not representative of the area, since the amount measured is related to the intensity of convective cells that pass directly over the gage location. Since the space and time resolutions of precipitation by weather radar observations are far superior to a reporting rain gage network, the problem of real-time observation of precipitation by radar has been largely alleviated in most of the eastern two-thirds of the United States. However, weather radar estimates of rainfall are generally limited to an area within 200 km of the radar in most locations and even less in mountainous areas.

In recent years, Stout et al¹ and Griffith et al² have had some success using visible and infrared geostationary satellite imagery for timely estimates of

(Received for publication 25 March 1981)

1. Stout, J. E., and Martin, D. W. (1979) Estimating GATE rainfall with geosynchronous satellite images, *Mon. Wea. Rev.* 107:585-598.
2. Griffith, C. G., Augustine, J. A., Woodley, W. L., and Meiten, J. G. (1980) The estimation of convective rainfall from thermal infrared, geosynchronous satellite data (to be published).

rainfall amounts over synoptic scale areas associated with deep convection over the tropical Atlantic Ocean. Although the satellite sensors do not directly sense precipitation-size particles, the success of these methods,^{1,2} is attributable to the physical mechanisms that produce the cumulonimbus cells and the accompanying cirrus anvils. The deep convection in cumulonimbus cells accounts for approximately 95 percent of the precipitation over the tropical oceans.³ Since the space and time scales of anvils generated by individual cumulonimbus clouds are on the order of tens of kilometers and 1 to 2 hours, the life cycle of the anvil growth and dissipation can be monitored by current geostationary satellites. Thus, it has been possible to develop statistical schemes to estimate rainfall on the basis of rate of growth and thickness of the cirrus anvil.^{1,2,4,5}

Little attention has been given to the use of geostationary satellite data for estimating precipitation in mid-latitude cyclonic storms where rainfall is produced by relatively shallow convection over synoptic scale areas. The reason is that in mid-latitude synoptic-scale systems, high-level stratiform clouds often prevent the satellite from observing the shallow convection. Nevertheless, geostationary imagery has been used successfully in delineating precipitating from nonprecipitating clouds⁶ and in estimating rainfall amounts from both deep and shallow convective clouds in the vicinity of Montreal.⁷ These studies show that the best satellite rainfall estimates, when compared to radar-estimated rainfall, were obtained when the IR channel of the geostationary satellite was used. The satellite rainfall estimates were adjusted empirically on the basis of the output from a cumulus-cloud model initialized with the observed thermodynamic structure at a nearby location. When tropical rainfall-estimation techniques were applied to mid-latitudes, the imagery failed to distinguish between light ($<2 \text{ mm h}^{-1}$) and heavy ($\geq 2 \text{ mm h}^{-1}$) mid-latitude rainfall areas. Also satellite imagery alone added little information in determining mid-latitude rainfall amounts. Radar

3. Houze, R.A., Jr., and Cheng, C.P. (1977) Radar characteristics of tropical convection observed during GATE: Mean properties and trends over the summer season, Mon. Wea. Rev. 105:964-980.
4. Scofield, R.A., and Oliver, V.J. (1977) A scheme for estimating convective rainfall from satellite imagery, NOAA Tech. Memo. NESS 86, Washington, D.C., 47 pp.
5. Woodley, W.L., Griffith, C.G., Griffin, J.S., and Stromatt, S.C. (1980) The inference of GATE convective rainfall from SMS-1 imagery, J. Appl. Meteorol. 19:388-408.
6. Lovejoy, S., and Austin, G.L. (1979) The delineation of rain areas from visible and IR satellite data for GATE and midlatitudes, Atmos.-Oceans 20:79-82.
7. Wylie, D.P. (1979) An application of a geostationary satellite rain estimation technique to an extratropical area, J. Appl. Meteorol. 18:1640-1648.

studies of mid-latitude cyclones in New England by Austin and Houze,⁸ and in England by Harrold and Austin⁹ revealed that within an extratropical cyclone, precipitation areas occur in a continuum of sizes, shapes, and intensities. At the large end of the continuum (1000 km), steady but light rainfall is produced by large-scale lifting (several centimeters) associated with the cyclonic circulation. At the other end of the continuum, the most intense rainfall is produced on small scales (1 to 10 km) characterized by buoyant parcels of air with relatively large vertical velocities (several meters per second). Between these extremes, radar studies have shown that mesoscale precipitation areas contain all of the convective cells, accounting for the majority of rainfall in cyclones. The work described in this study is an attempt first, to identify from satellite imagery those mesoscale features observed by radar during rain events that contained relatively shallow convection; and second, to determine how accurately the current geostationary satellite sensors resolve these mesoscale features.

2. MESOSCALE STRUCTURE OF PRECIPITATION WITHIN EXTRATROPICAL CYCLONES

The highly organized nature of mesoscale precipitation patterns in mid-latitude cyclonic storms was first noted by Austin and Houze⁸ in New England, and Harrold and Austin⁹ in England. Their studies show that subsynoptic-scale features form the basic components of most precipitation patterns and that these features have clearly definable characteristics and behavior. There is one important aspect of these findings: that the horizontal distribution of precipitation in cyclonic storms of all types tends to form in mesoscale bands or lines generally parallel to the frontal surfaces. The mesoscale rainbands occur with varying intensities in different cyclones and may not all be present in a particular cyclone.

Precipitation patterns within the rainbands also show organization and coherence on the small mesoscale (areal extend of 50 to 10,000 km²). Radar studies have shown that small-scale precipitation patterns on the small mesoscale tend to have preferred sizes and that each small mesoscale area behaves as if it were a distinct entity. The proposed areal extents of mesoscale precipitation areas based on the findings of Austin and Houze⁸ and Reed¹⁰ are illustrated in Figure 1.

8. Austin, P.M., and Houze, R.A., Jr. (1972) Analysis of the structure of precipitation patterns in New England, J. Appl. Meteorol. 11:926-935.
9. Harrold, T.W., and Austin, P.M. (1979) The structure of precipitation systems—A review, J. de Rech. Atmos. 8:41-57.
10. Reed, R.W. (1972) Characteristics and Development of Mesoscale Precipitation Area in Extra-tropical Cyclones, SM Thesis, Dept. of Meteorology, M.I.T., Cambridge, Massachusetts, 94 pp.

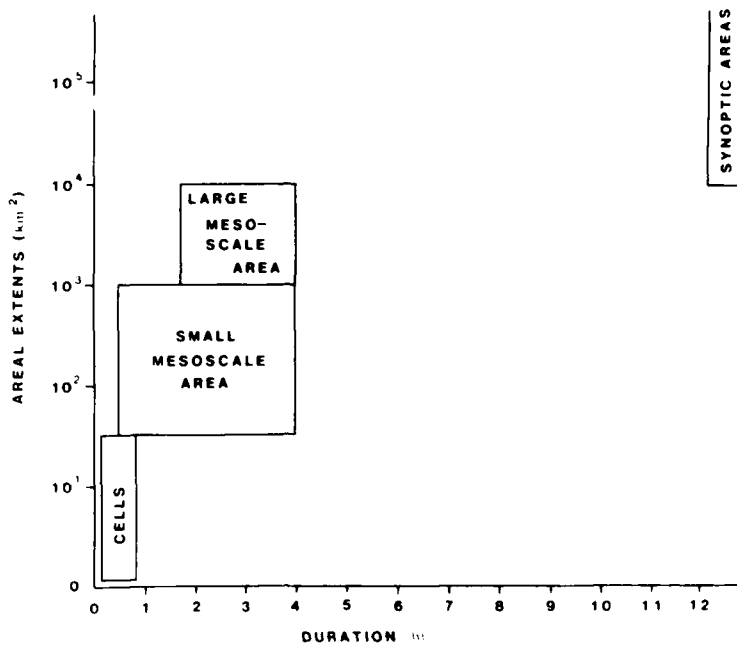


Figure 1. Proposed Areal Extent of Mesoscale Precipitation Areas. They are based on findings of Austin and Houze⁸ and Reed¹⁰

Within most mesoscale rainbands, the movement and behavior of small mesoscale areas (SMSAs) are closely related to the cellular activity within them. A SMSA is defined as a region of precipitation 50 to 1000 km^2 with a radar reflectivity level above 34 dBZ ¹¹ that contains at least one convective cell, although several cells are usually present. Convective cells are generally the smallest precipitation elements observable by radar; they are normally embedded within a SMSA, or in a cluster of radar echoes forming an area similar in size to a SMSA. The convective cells range in size from less than 0.5 km to a few kilometers in thunderstorms, with associated rainfall rates ranging from a few millimeters per hour to as much as 100 mm h^{-1} . The spatial and temporal scales of most non-cumulonimbus cells in extratropical cyclones preclude detection by current and planned polar or geostationary satellites.

A large mesoscale area (LMSA) is defined as a region of precipitation 1000 to $10,000 \text{ km}^2$ with a radar reflectivity level above 30 dBZ ¹¹ and generally consists of one or more SMSAs. The movement of LMSAs is more closely related

11. Bjerkaas, C. L. (1977) Mesoscale Characteristics of Precipitation in a Disturbance of the Tropical Eastern Atlantic, SM Thesis, Dept. of Meteorology, M.I.T., Cambridge, Mass., 104 pp.

to the movement and behavior of the larger scale rainband than to that of the SMSAs. Figure 2 is a schematic of a LMSA containing two SMSAs which have cells embedded within them. Note that the cells do not necessarily have to be embedded within SMSAs but are generally within the LMSA. One must bear in mind that these areas continually change in form, size, and intensity with time. The precipitation intensity for cells is generally two to ten times greater than the average rate for SMSAs, which, in turn, is twice the over-all rainfall intensity of LMSAs. The average precipitation intensity in LMSAs is about twice the synoptic-scale rainfall intensity. Although cells have by far the largest rainfall intensity, Austin¹² found that SMSAs and LMSAs were the major contributors to total rainfall volume in extratropical cyclones. Therefore, in order to estimate rainfall totals accurately with satellite imagery on the mesoscale, it is essential that

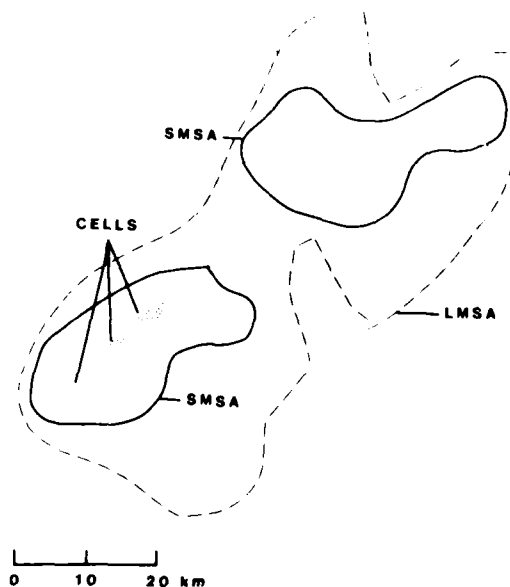


Figure 2. Schematic of Mesoscale Areas. Cells (stippled areas), two SMSAs (solid lines) within a LMSA (dashed line). The contours outlining each feature can be considered to indicate radar reflectivity levels or rainfall rates

12. Austin, P. M. (1978) Characteristics of rain echoes defined by a threshold intensity, 18th Conference on Radar Meteorology, Amer. Meteor. Soc., Boston, Massachusetts, 165-170.

satellite sensors adequately resolve SMSAs and LMSAs. Figure 1 suggests that that spatial and temporal scales of both SMSAs and LMSAs are large enough to detect and monitor with the sensors aboard geostationary satellites.

3. CASE STUDY OF THREE NEW ENGLAND RAIN EVENTS

3.1 Selection of Cases

Cases of precipitation were selected from available coincident radar, satellite, and hourly rain gage data for the rare instances when higher clouds did not hide the LMSA and SMSA from the satellite sensors. Analysis was restricted to midday hours to eliminate the need for brightness normalization of the visible satellite imagery. Table 1 lists the dates and periods selected for analysis.

Table 1. Dates and Time Periods Used in This Study

Date	Rain Gage Time (GMT)	Satellite Time (GMT)	Radar Time (GMT)
19 April 1978	1600-2000	1600-2000	1602-2153
5 May 1978	1500-2000	1500-2000	1512-2017
15 May 1978	1600-2000	1600-2000	1609-2017

3.2 The Data Bases

Digital radar data used in this study were taken by the calibrated WR66 and WR72 weather radars operated by the Department of Meteorology at the Massachusetts Institute of Technology (MIT). Characteristics for both radars are given in Table 2 and a list of nominal radar-map times used in this study in Table 3. The mean temporal resolution of the radar data on 19 April was 12 minutes, on 5 May, 19 minutes, and on 15 May, 21 minutes. On the average, five elevation angles were taken on the 19 April radar maps, three on 5 May, and four on 15 May. The number of elevation angles scanned by the radar is dependent upon depth of the precipitation echoes, and the distance between precipitation echoes and radar at the time of the scans.

The digital radar data were stored on McIDAS (Man-computer Interactive Data Access System) disk files* in B-scan format, a format that treats the radar

* Air Force Geophysics Laboratory (AFGL).

Table 2. Characteristics of MIT WR66 and WR73 Weather Radars

	WR66	WR73
Wavelength (cm)	10.5	5.5
Frequency (MHz)	2850	5550
Beam Width (degrees between half-power points)	1.35	1.40
Pulse Length (μ sec)	1.0	2.0
Nominal Transmitted Power (kW)	600	250
Range (km)	200	200

Table 3. Time of Radar Maps for the Three Selected Cases

Date	List of Times (GMT)	Radar Used
19 April 1978	1602, 1612, 1622, 1632, 1636, 1647, 1657, 1707, 1717, 1727, 1747, 1758, 1819, 1832, 1842, 1852, 1902, 1912, 1922, 1937, 1947, 1957, 2007, 2007, 2017, 2049, 2059, 2143, 2153	WR66
5 May 1978	1512, 1527, 1557, 1612, 1627, 1642, 1717, 1728, 1743, 1758, 1813, 1943, 1932, 1947, 2002, 2017	WR73
15 May 1978	1609, 1624, 1710, 1725, 1740, 1758, 1817, 1832, 1847, 1917	WR66

data in R , θ coordinates as if these were rectangular with X being R and Y being θ . Although gross visual distortions occur with this format, it was the most convenient method for examining the data. The radar data were processed using the McIDAS facility for all elevation angles in such a manner that each geographical point in the B-scan format contained the maximum signal returned to the radar. This procedure tends to overestimate the rainfall at the ground. Although the precipitation at the highest elevation angles may not reach the ground, accurate positioning of the more intense precipitation allowed one to locate accurately areas of precipitation in the satellite imagery.

Based on the radar thresholding work of Freeman¹³ and Bjerkaas,¹¹ precipitation areas were identified at sequential intensity thresholds. The radar data in the B-scan array were first scanned to find the maximum signal returned to the radar. The radar threshold is adjusted in such a manner that the last four thresholds processed are 38, 34, 30, and 26 dBZ. The minimum detectable signal of both MIT radars is 26 dBZ. The thresholds approximately delineate cells (38 dBZ), SMSAs (34 dBZ) and LMSAs (30 dBZ). Once the entire radar array has been scanned at the adjusted threshold, the threshold is decremented by four, and a scan through the data repeated for the new threshold until the 26 dBZ threshold has been processed. The radar data were processed in 4 dBZ increments from 26 dBZ to the maximum observed value. The areal coverage, area-weighted centroid of the echo (in polar coordinates) and the precipitation mass flux were computed for each increment. This manner of processing allows examination of all scales and intensities of echoes, although only the final four thresholds (38, 34, 30 and 26 dBZ) were used in this study. The entire B-scan map was searched in order to locate areas of precipitation. Any point within 37 km of the radar were considered ground clutter, and eliminated before searching for echoes.

The satellite imagery were taken by the Geostationary Operational Environmental Satellite (GOES) visible sensor (sensitive to reflected radiation in the 0.55- to 0.75-micron range) and IR sensor (sensitive to thermal radiation in the 10.5 to 12.6 micron range). The 1 km visible and 4 km IR half-hourly satellite imagery were obtained from the Space Science and Engineering Center (SSEC) at the University of Wisconsin, Madison. Table 4 is a list of the satellite observation times used in this study. Neither sensor directly detects precipitation-size particles. The sensors respond mainly to reflected and thermal radiation from the numerous small particles 1 to 100 microns in size and only slightly to precipitation particles 100 to 5000 microns. When the cloud particles are actively growing to precipitation-size particles, the cloud particle concentration increases substantially, allowing more reflection of visible radiation. The higher cloud particle concentration also decreases the amount of terrestrial radiation passing through the clouds, making them appear colder. Therefore, precipitating clouds appear brighter and colder than nonprecipitating clouds.

Hourly rain gage data were obtained from the Air Weather Service's Environmental Technical Applications Center (ETAC) in Asheville, North Carolina. The strip charts from recording rain gages were manually converted to hourly rainfall amounts and stored onto computer tapes at ETAC. Cooperative observation rain

13. Freeman, L. E. (1976) Sizes and Intensities of Mesoscale Precipitation Areas as Depicted by Digital Radar Data, SM Thesis, Dept. of Meteorology, M.I.T., Cambridge, Massachusetts, 96 pp.

gage sites, located throughout the New England and eastern New York region, have an average distance of 5 km between sites.

Table 4. Time of Satellite Images Used in the Three Cases

Date	Times (GMT) of Visible and Infrared Imagery	Satellite
19 April 1978	1600, 1630, 1700, 1730, 1800 1830, 1900, 1930	GOES-2
5 May 1978	1500, 1530, 1600, 1630, 1700 1730, 1800, 1830, 1900, 1930 2000	GOES-2
15 May 1978	1600, 1630, 1700, 1730, 1800 1830, 1900, 1930, 2000	GOES-2

3.3 Characteristics of the Precipitation

Radar constant altitude plan position indicator (CAPPI)^{*} scans for the three cases showed that the precipitation was confined to the lowest 5 to 6 km of the atmosphere. This is consistent with the generally stable conditions evident in New England and eastern New York soundings that were examined. The 19 April radar CAPPI scans showed that a pre-warm frontal rainband extended along a northwest-southeast line and intensified as the band moved toward the northeast over New England. On 15 May, the radar CAPPI scans showed that the precipitation in New England was associated with an east-west oriented pre-warm frontal rainband that moved northeastward during the 4-hour period radar data were available. The precipitation on 5 May was not organized in a mesoscale rainband as in the other two cases. Satellite data for all three cases were examined in detail to determine if differences in the imagery exists between this day and the two days with mesoscale organization.

Radar and hourly rain gage data showed that precipitation was light in each of the cases. Less than 0.5 percent of the rain gages recorded greater than 0.05 in h^{-1} for all three cases combined. In addition to the precipitation being generally light on all three days, the percentage of stations measuring rain varied significantly between the three cases. On 19 April, measurable rain was reported in about 35 percent of the hourly observations, while on 5 May and 15 May,

^{*} Radar scans of various elevation angles are processed yielding a Plan Position Indicator (PPI) radar map at selective heights.

approximately 6 percent and 10 percent respectively of the hourly observations had measurable rain. Table 5 lists the grand totals of rainfall rates for all three days.

Table 5. Frequency of Rainfall Rates for All Stations, for Each Case, and for All Three Cases

		Rainfall Rate (in h^{-1})			
		None	0.01	0.02-0.05	0.06-0.10
19 April	318	184	26	5	0
5 May	430	26	0	0	0
15 May	619	60	11	2	0
Total	1367	270	37	7	0

The distribution of hourly rainfall amounts, radar reflectivity levels and clouds in the satellite images show that precipitation in New England on 19 April and 15 May, was a result of shallow mesoscale convection. Based on examination of the surface and upper air maps, precipitation occurred in a pre-warm frontal rainband. The sounding data showed that cloud tops were generally between 5 and 6 km, with little or no cloud above this level. The satellite images examined also supported the absence of a high cloud layer, permitting a direct view of the lower level precipitating clouds in the rainbands.

4. RESULTS OF RADAR ANALYSES

The characteristic space and time scales of the precipitation areas that occurred during the three cases were examined with digitized radar data, in order to establish whether they were large enough for detection by the satellite-sensors. With the radar thresholding study of Freeman¹² as a guide, the processed radar data were examined to determine first, the spatial and temporal scales of major echoes (radar echoes ≥ 26 dBZ that reached at least 1000 km^2 in size), the LMSAs (>30 dBZ) and SMSA (>34 dBZ), and second, the relative contribution by cells (>26 dBZ), SMSAs and LMSAs to the total (all echoes >26 dBZ) precipitation of the major echoes. Four major echoes occurred on 19 April and one on 15 May. Table 6 lists the initial and final times that the echoes were observed on the B-scan maps. Some small, scattered echoes were visible on the 5 May B-scan maps, but none achieved even the size of SMSAs.

Table 6. Temporal Summary of the Five Major Echoes Detected by Radar for 19 April and 15 May 1978. A plus (+) sign preceding the time signifies that the echo was probably presented prior to the first available radar map and a plus sign following the time indicates that the radar echo probably extended beyond the last available radar map

Date	Designation	Initially Observed (GMT)	Finally Observed (GMT)	Duration (minutes)
19 April	A	1622	2007	225
19 April	B	1707	2017	190
19 April	C	1852	2153+	181+
19 April	D	1937	2153+	136+
15 May	E	+1609	1917+	+188+

4.1 Characteristics of Mesoscale Features

The duration of SMSAs and LMSAs within the five major echoes appear in Table 7. Echoes depicted by the 30-dBz threshold and within the size range of 1000 to 10,000 km² were labeled as LMSAs, whereas echoes depicted by the 34-dBZ threshold which reached a size between 50 to 1000 km² were labeled as SMSAs. Although echo A did not contain any SMSAs or LMSAs, the remaining major echoes contained at least one LMSA and two SMSAs. The average duration of all SMSAs was 49 minutes and for all LMSAs, 90 minutes. While these lifetimes agree with the duration for SMSAs and LMSAs proposed by Austin and Houze,⁸ and Reed,¹⁰ they are at the lower end of the range of lifetimes. Although the average lifetime of some SMSAs was small, the mean duration of SMSAs, LMSAs, and major echoes indicate that half-hourly satellite images would be sufficient for detecting these areas.

The time variation of the area enclosed by echoes A, B, C, D, and E, and the SMSAs and LMSAs within the major echoes appear in Figures 3 through 7, respectively. These figures show that the spatial scales of major echoes and of LMSAs and SMSAs within them are sufficiently large to be detected by current geostationary satellite sensors (4 × 8 km IR and 1.5 × 2 km visible sensor resolution).

Table 7. Temporal Summary of SMSAs and LMSAs Within the Five Major Echoes Detected on 19 April and 15 May 1978. Plus (+) signs have the same meaning as in Table 6

Echo Area Designation	Type	Time Initially Observed (GMT)	Time Finally Observed (GMT)	Duration (minutes)
A	SMSA	None		
A	LMSA	None		
B	SMSA	1819	1852	33
B	SMSA	1842	1922	40
B	LMSA	1819	1902	43
C	SMSA	1937	2039	62
C	SMSA	2059	2143	44
C	SMSA	2059	2153	54+
C	LMSA	1937	2153	136+
D	SMSA	2039	2059	20
D	SMSA	2039	2059	20
D	LMSA	2017	2059	42
E	SMSA	1609	1710	61
E	SMSA	1624	1710	46
E	SMSA	1624	1847	143
E	SMSA	1740	1758	18
E	LMSA	1609	1832	143

4.2 Rainfall Characteristics of Mesoscale Features

The vertical mass flux ($m^3 sec^{-1}$) of precipitation for each 2 km square area within the echo was computed from the radar data using

$$Z = 232R^{1.25}$$

where Z is radar reflectivity and R rainfall rate.¹⁴ This Z-R relation is appropriate for the types of storm cases examined in this study. Precipitation mass

14. Personal correspondence with Spiros G. Geotis of the M.I.T. Weather Radar Office.

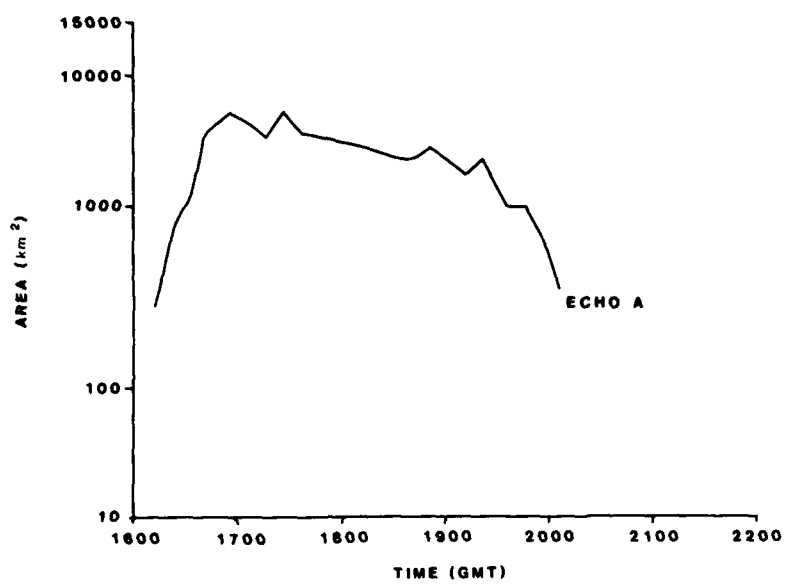


Figure 3. Echo A Area Summary

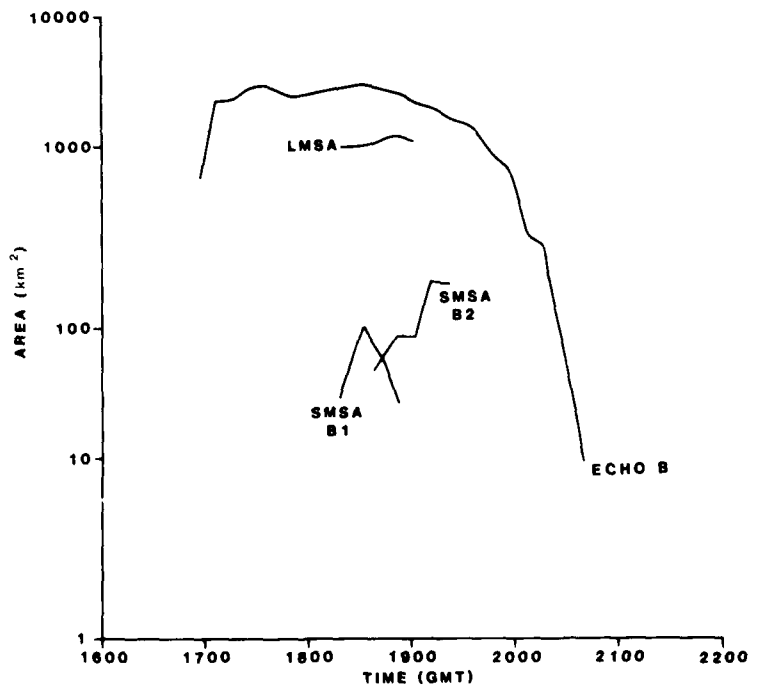


Figure 4. Echo B Area Summary

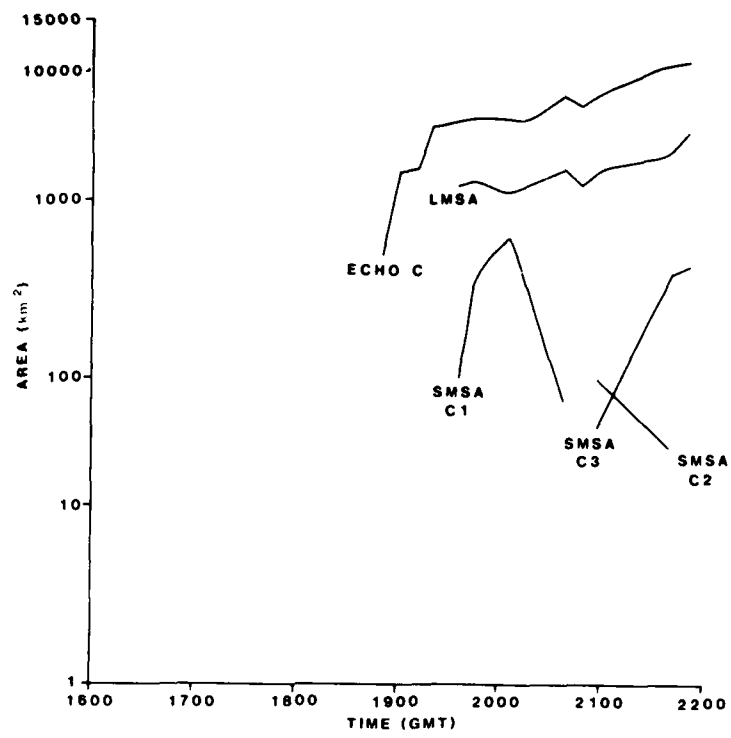


Figure 5. Echo C Area Summary

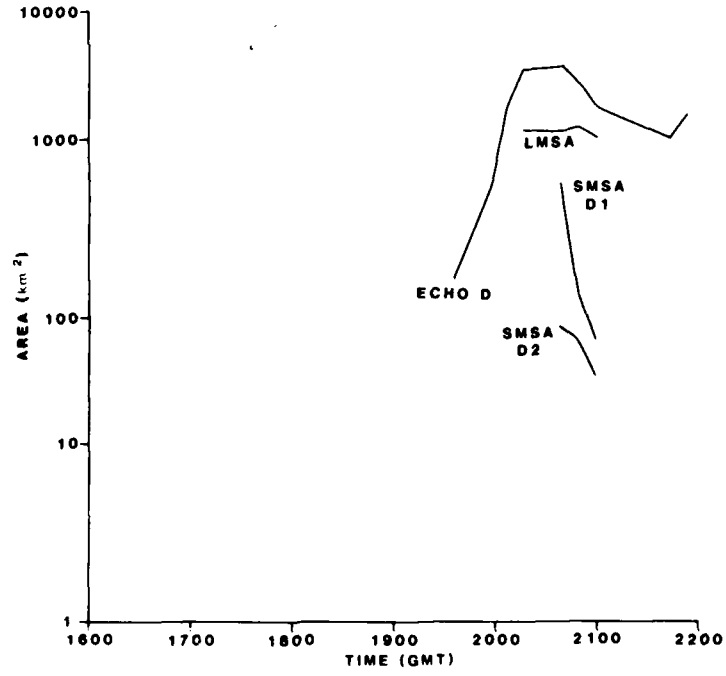


Figure 6. Echo D Area Summary

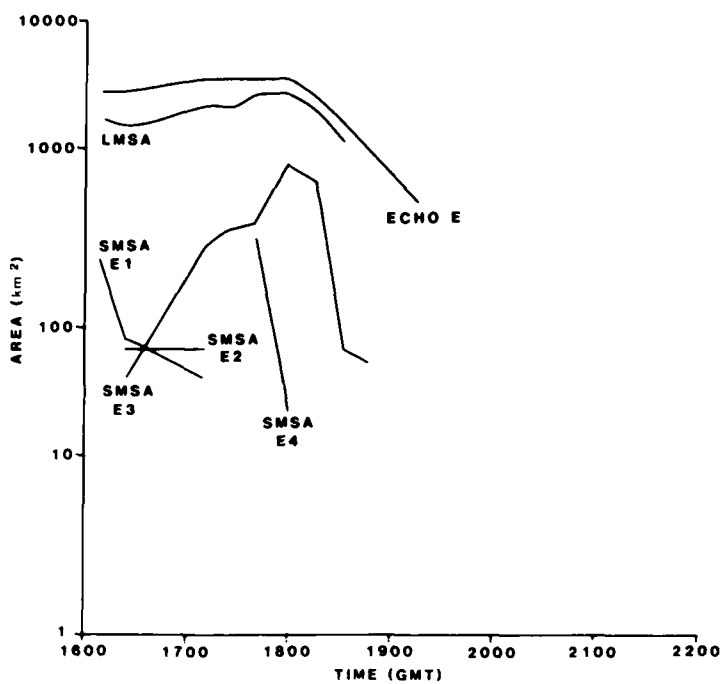


Figure 7. Echo E Area Summary

flux was used to estimate the relative contribution of rainfall by major echoes to the total estimated precipitation sensed by the radar. In addition, it was used to estimate the contribution by cells, SMSAs and LMSAs to each of the major echoes. Computation of precipitation mass flux for cells, SMSAs, LMSAs and major echoes involved summing the mass flux contribution of each 2 km square area within the radar threshold areas. Tables 8a and 8b list the percentage contributions of mass flux by the major echoes to the total mass flux of each radar map for 19 April and 15 May, respectively. On the average, three quarters of the total mass flux of each radar map on 19 April is accounted for by the major echoes, whereas on 15 May only 40 percent of the total mass flux is accounted for by major echo E. The 35 percent difference between the two days is largely explained by the presence of a larger number of smaller echoes (generally less than 100 km^2) on 15 May.

The relative contributions to the mass flux of major echoes A, B, C, D, and E by cells, SMSAs and LMSAs appear in Figures 8 through 12. On the average 33.9 percent of the mass flux of major echoes was contributed by LMSAs, 13.4 percent by SMSAs, and only 5.5 percent by cells on 19 April. For 15 May, 47.5 percent of the mass flux of major echo E was contributed by the LMSA, 37.6 percent by SMSAs and 12.2 percent by cells within the echo. (On each day, the remainder of the mass flux for each major echo was contributed by measurable

Table 8a. Percentage Contribution to Total Mass Flux of Radar Map by the Major Echoes for 19 April 1978

Time (GMT)	Major Echoes Present at Map Time	Percentage Mass Flux by Combined Major Echoes
1612	A	11.2
1622	A	28.4
1632	A	32.8
1636	A	73.5
1647	A	74.2
1657	A, B	74.9
1707	A, B	64.5
1717	A, B	73.1
1727	A, B	89.2
1737	A, B	82.1
1747	A, B	86.2
1758	A, B	86.9
1819	A, B	85.6
1832	A, B	82.3
1842	A, B	83.5
1852	A, B, C	82.1
1902	A, B, C	80.0
1912	A, B, C	72.5
1922	A, B, C	89.3
1937	A, B, C, D	86.4
1947	A, B, C, D	86.0
1957	A, B, C, D	80.0
2007	A, B, C, D	76.2
2017	A, C, D	93.3
2039	A, C, D	94.6
2049	C, D	85.1
2058	C, D	82.9
2143	C, D	80.5
2153	C, D	77.2

Table 8b. Percentage Contribution to Total Mass Flux of Radar Map by the Major Echoes for 15 May 1978

Time (GMT)	Major Echoes Present at Map Time	Percentage Mass Flux by Combined Major Echoes
1607	E	38.8
1624	E	32.8
1710	E	44.0
1725	E	44.7
1740	E	46.8
1758	E	46.7
1817	E	45.3
1832	E	39.5
1847	E	41.2
1917	E	19.1

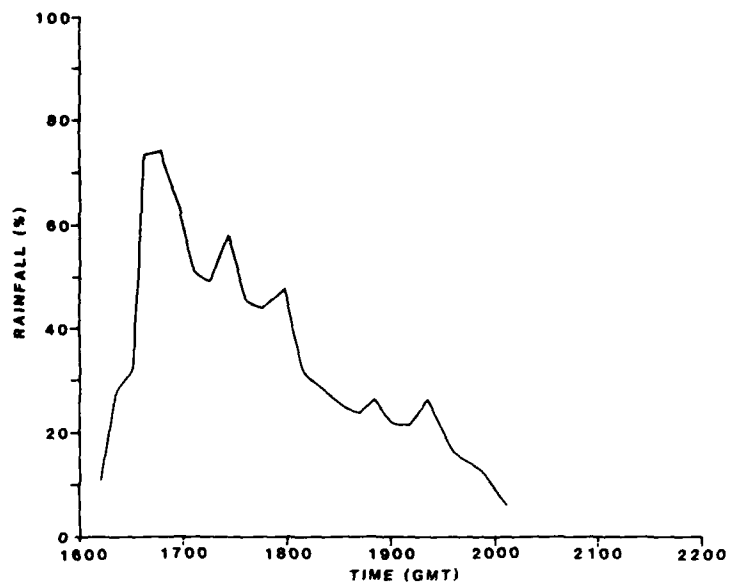


Figure 8. Contribution of Major Echo A to Total Estimated Rainfall

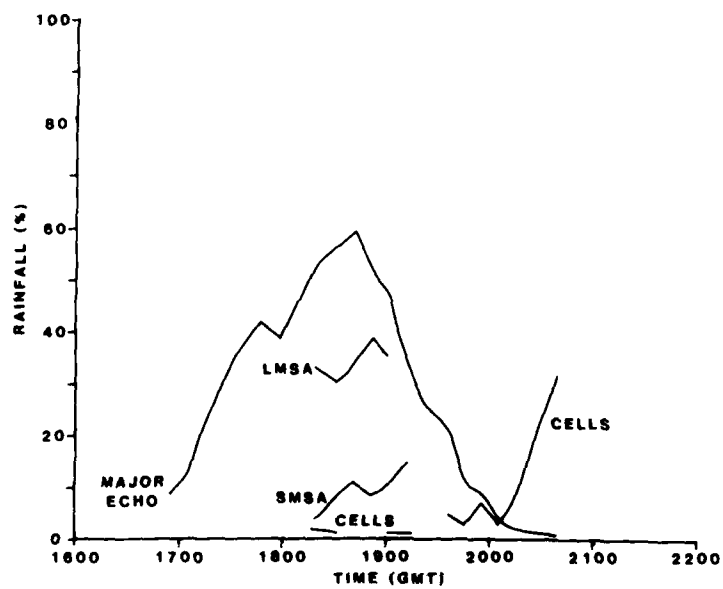


Figure 9. Contribution of Major Echo B to Total Estimated Rainfall and Contribution by Mesoscale Features to Major Echo B

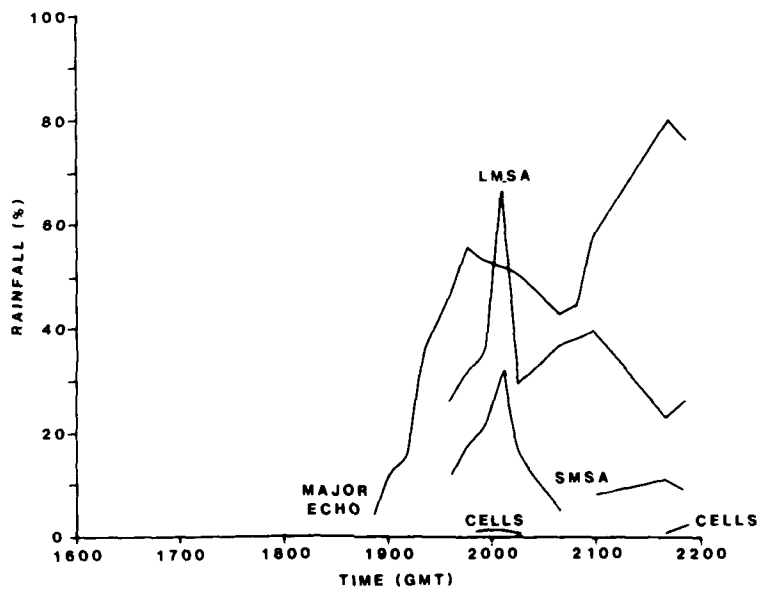


Figure 10. Contribution of Major Echo C to Total Estimated Rainfall and Contribution by Mesoscale Features to Major Echo C

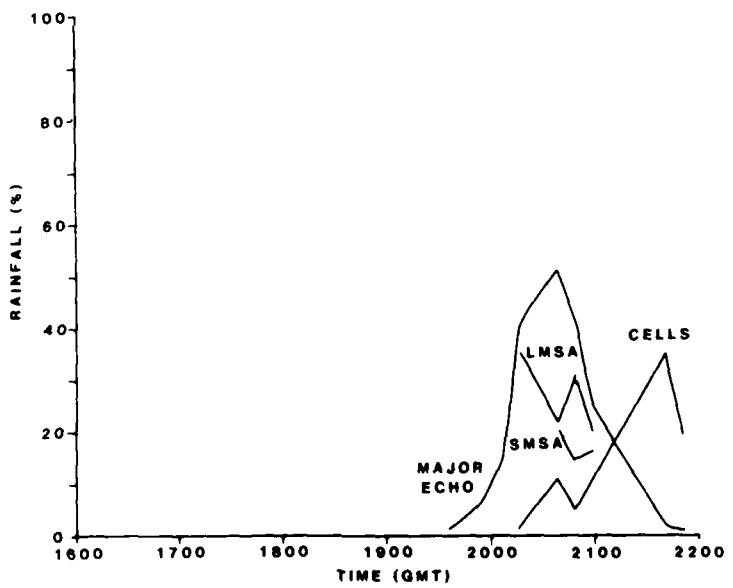


Figure 11. Contribution of Major Echo D to Total Estimated Rainfall and Contribution by Mesoscale Features to Major Echo D

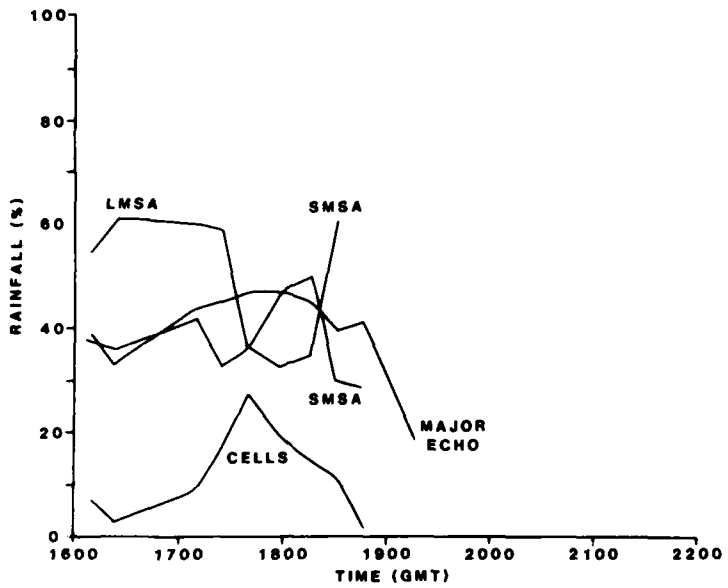


Figure 12. Contribution of Major Echo E to Total Estimated Rainfall and Contribution by Mesoscale Features to Major Echo E

radar reflectivity levels that did not meet the criteria of cells, SMSAs, or LMSAs.

Figures 8 to 12 show the rainfall contribution by the cells to the total mass flux of each major echo. With the exception of the dramatic fluctuations in mass flux contributed by cells (for example, 32 percent at 2039 GMT for echo B), the contribution by the cells is so small that it could be neglected without dramatically affecting an average areal estimate of rainfall for synoptic-scale areas. This is encouraging since the short duration of cells preclude monitoring them on current geostationary satellite imaging intervals.

The question of the importance of the SMSAs to the total mass flux is not adequately resolved in this study since the results are very different on 19 April and 15 May. On 19 April, the SMSAs account for 13 percent of the total mass flux, while on 15 May the SMSAs contributed 38 percent of the total mass flux. Analysis of additional cases that contain SMSAs are needed to understand better the contributions SMSAs make to the total mass flux of mesoscale rainbands.

5. RESULTS OF SATELLITE DATA ANALYSIS

Satellite meteorologists have long been aware that rain producing clouds in the tropics are generally brighter (visible) and colder (IR) than nonprecipitating clouds. Muench and Keegan¹⁵ developed a similar relationship between precipitation and satellite-observed cloud brightness and temperature in mid-latitude stratiform clouds. In this study, therefore, GOES visible and IR imagery were examined to determine if, in the absence of higher layered clouds, rain producing clouds could be separated from surrounding nonprecipitating clouds on the basis of brightness and temperature.

5.1 Satellite and Rain Gage Comparisons

The McIDAS facility at AFGL was used to process all the satellite images of 19 April, 5 May, and 15 May 1978. Navigated visible and IR pairs of GOES imagery over New England for all three dates were loaded into McIDAS and displayed on the television monitor. The satellite images covered an area within a 40°N to 45°N and 68.4°W to 74.5°W latitude-longitude box. Visual inspection of all images for the three days indicated that on 19 April and 15 May, the IR imagery showed that in the general vicinity of the centroid of the major echoes established by radar, the clouds were somewhat colder. Corresponding visible images indicated that clouds in the immediate vicinity of the major echoes were generally no brighter than those in other parts of the image. In essence, visual inspection of all imagery indicated that on 19 April and 15 May, thermal thresholding of the IR imagery might be able to delineate precipitating from nonprecipitating clouds. However, on 5 May, the generally uniform IR radiances in raining and nonraining areas prevented the delineation of regions with precipitation. The superposition of the rain gage data onto the satellite imagery showed that the relatively colder clouds sensed in the IR channel on 19 April and 15 May, were located in the general areas where rainfall occurred. On 5 May the uniform IR radiances showed no delineating capability when the rain gage data were overlayed onto the images.

5.2 Delineation of Rainfall Areas by Thresholding the Satellite Imagery

A first guess of an optimum threshold was made for each day separately, by examining the frequency distributions of visible and IR digital counts of each image viewed on the McIDAS television monitor. The frequency distributions of visible

15. Muench, H. S., and Keegan, T. J. (1979) Development of Techniques to Specify Cloudiness and Rainfall Rate Using GOES Imagery Data, AFGL-TR-79-0255, AD A084 755, Bedford, Massachusetts, 46 pp.

counts for all three dates essentially were normally distributed and centered in the vicinity of the mean visible counts for the images. The IR frequency distribution of 5 May had a similarly shaped curve centered near the mean. However, the shape of the 19 April and 15 May IR frequency distributions were more bimodal. Figure 13 represents a typical IR frequency distribution for the days of 19 April and 15 May. The mode at the lower digital counts in Figure 13 is located in the vicinity of the mean IR digital count of the image. Based on rain gage measurements overlayed onto the satellite images, the mode located at the higher end of the distribution appeared to represent the precipitating clouds. The minimum between the two modes was used as a first guess of the IR threshold. The McIDAS was used to manipulate the IR data to allow more detailed analysis. The region of IR counts at and above the threshold were linearly rescaled (stretched) to the full digital range of the satellite imagery (1-255) and displayed. By overlaying the rain gage measurements over the satellite display, one made adjustment of the first guess threshold to obtain the final threshold that best separated small rain areas from larger areas with little or no precipitation.

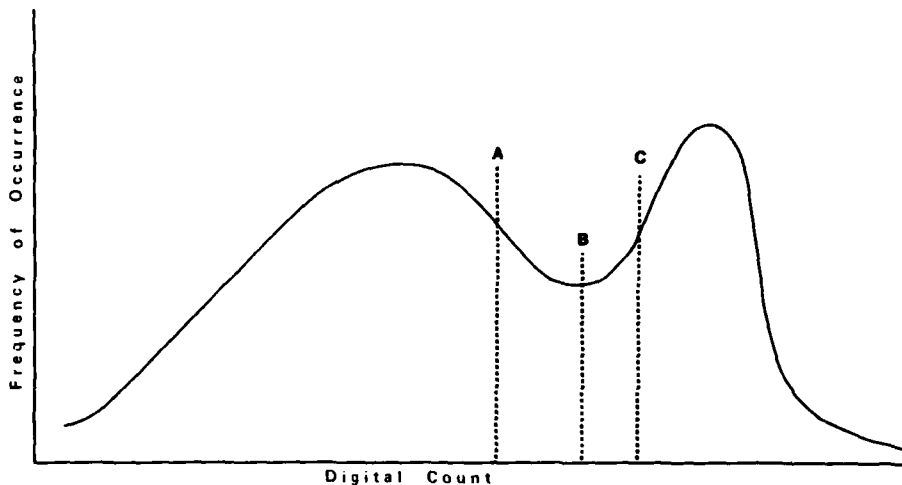


Figure 13. Typical IR Frequency Distribution 19 April and 15 May. Line A represents the mean IR count for the image. Line B is the first guess IR threshold. Line C represents the final adjusted IR threshold that best separated precipitating from nonprecipitating clouds. The curve in this figure has been smoothed for clarity.

The IR threshold, on the average, on 19 April was an IR digital count of 172 (-29.0°C) and for 15 May it was the 175 IR digital count (-30.5°C). If the IR radiances represent cloud-top temperatures (assuming the clouds radiate as black bodies), then the digital IR count (or temperature) of the threshold can be compared to the vertical temperature structure depicted by a representative sounding for the area and day. On 19 April, -29°C corresponds to a height of approximately 7.2 km, while on 15 May, -30.5°C corresponds to a height of approximately 7.5 km for the cloud top. This is in reasonable agreement with the radar detected heights of echoes resulting from precipitation-size particles.

5.3 Satellite Threshold and Rain Gage Comparisons

The IR count data were rescaled at and above the refined thresholds (172 on 19 April and 175 on 15 May) using McIDAS, in order to make comparisons with the rain gage data. Figures 14 and 15 illustrate typical correspondence between the IR threshold area and precipitation detected by radar ($\geq 26 \text{ dBZ}$). Although the area enclosed by the satellite IR threshold is generally larger than the area depicted by the 26 dBZ contour, there is agreement in terms of general shape and orientation.

Rain areas defined by the satellite IR threshold were compared with rain gage records for the hour ending at image time. The degree of agreement between them was evaluated with an interactive procedure developed on McIDAS for this study. Tables 9a and 9b and 10a and 10b summarize the results for those rain gages within and without the IR threshold for 19 April and 15 May respectively. On 19 April, 89 percent of the rain gages that reported precipitation are within the satellite threshold area, while on 15 May, only half are within the satellite threshold area. However, due to the rapid northeastward movement of the rainband on May 15, approximately half of the rain gages with measurable rain outside the IR threshold area were within 30 km south of the threshold area. The results illustrated in Figures 14 and 15, together with Tables 9a and 9b, and 10a and 10b, show that in the absence of higher layered clouds, IR satellite imagery is capable of delineating precipitating from nonprecipitating cloud areas. This outcome is consistent with the Montreal studies of Lovejoy and Austin,⁶ and Wylie.⁷

5.4 Satellite and Radar Comparisons

Within the IR area enclosed by the subjectively determined thresholds (172 and 175 for 19 April and 15 May, respectively), colder IR temperatures (higher IR digital counts) corresponded more closely to the areas enclosed by the major radar echoes. The time variation of both major radar echo areas and the mass

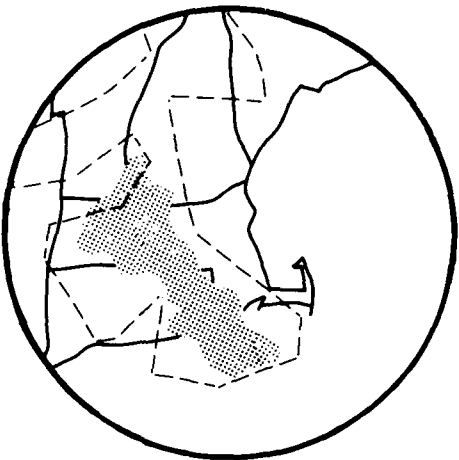


Figure 14. The 1800 GMT, 172 IR Digital Count Satellite Threshold Area (dashed line) and the 1758 GMT, 26-dBZ Radar Reflectivity (stippled area) on 19 April 1978. Note the similar orientation and general shape between satellite depicted threshold and radar area

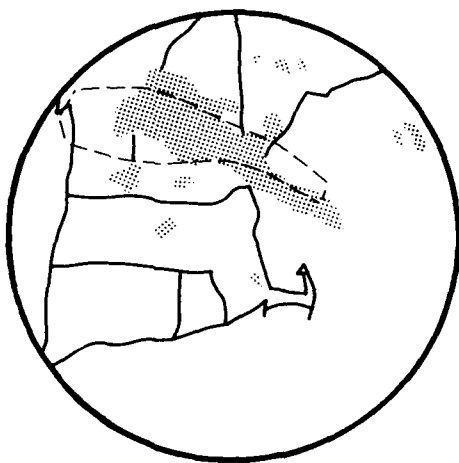


Figure 15. The 2000 GMT, 175 IR Digital Count Satellite Threshold Area (dashed line) and the 2002 GMT, 26-dBZ Radar Reflectivity Level (stippled area) on 15 May 1978. Note the similar orientation and general shape between satellite depicted threshold and radar area

Table 9a. Frequency Distribution of Rainfall Rates Inside Optimum IR Threshold Area for 19 April 1978

Time (GMT)	Rainfall Rate (in h^{-1})			
	None	0.01	0.02-0.05	0.06-0.10
16	52	26	1	0
17	57	29	5	0
18	43	33	5	1
19	54	27	9	2
20	48	50	4	2

Table 9b. Frequency Distribution of Rainfall Rates Outside Optimum IR Threshold Area for 19 April 1978

Time (GMT)	Rainfall Rate (in h^{-1})			
	None	0.01	0.02-0.05	0.06-0.10
16	31	6	0	0
17	22	3	0	0
18	28	6	0	0
19	20	2	1	0
20	6	5	1	0

flux of rain was compared to the time change of these colder IR areas. This comparison was designed to determine if there is a relationship between the time variation of the colder IR satellite areas and variations of the radar areas (that is, the mesoscale areas). The procedure involved using the McIDAS facility to isolate each major echo and compute the area containing all image elements at the IR digital count (IRDC) that most closely corresponded to the area of the major echo. This procedure was then repeated for each digital count greater than the IRDC up to the maximum count observed for each major echo. For example, with echo A on April 19, the area within the digital count of 185 (the IRDC for radar echo A) was determined. Then the area for each digital count from 186

Table 10a. Frequency Distribution of Rainfall Rates Inside Optimum IR Threshold Area for 15 May 1978

Time (GMT)	Rainfall Rate (in h^{-1})			
	None	0.01	0.02-0.05	0.06-0.10
15	22	7	3	0
16	38	4	1	1
17	19	9	1	0
18	16	5	0	0
19	23	3	0	0
20	14	2	0	0

Table 10b. Frequency Distribution of Rainfall Rates Outside Optimum IR Threshold Area for 15 May 1978

Time (GMT)	Rainfall Rate (in h^{-1})			
	None	0.01	0.02-0.05	0.06-0.10
15	72	8	4	0
16	64	6	2	0
17	82	4	0	1
18	90	5	0	0
19	86	4	0	0
20	98	2	0	0

to the maximum digital count of 194 was computed for each available satellite image. This was also done for each of the four remaining major echoes. Satellite IR areas were determined for the digital counts from 175 to 183 for echo B, 180 to 188 for echo C, 193 to 200 for echo D and 172 to 178 for echo E. Thus, the IRDC for the five major radar echoes were 185, 175, 180, and 193 on 19 April and 172 on 15 May.

Then, the change in area between successive satellite IR images for each digital count at and above the IRDC, and the change in area between radar echoes

at corresponding satellite times were computed for each major echo. Thus, a rate of change in area was determined for the selected satellite digital counts and major radar echoes. A correlation analysis was then made between the time change of IR areas and the time variation of the major radar echo areas. The average correlation coefficient of the time change of IR and radar echo areas for all major echoes was 0.06. A correlation analysis was also made between the time change of radar estimated mass flux of rain for each major echo and the time variation of the IR areas (again, at and above the IRDC for each major echo). Here, the average correlation coefficient was 0.10 for all major echoes. Table 11 lists the correlation coefficients of satellite IR areas to both radar echo areas and precipitation mass flux of the major echoes. These data indicate that GOES IR imagery cannot detect time variations in the areas of the major echoes or the time changes in the mass flux of rain as determined by radar. In addition, within the major echoes the heavier rainfall amounts determined by radar were not always in the same location as the colder IR areas (see Figure 16) at corresponding times.

Because of the lack of correlation and the displacement between satellite and radar areas, statistical calibration of the satellite for rainfall estimation purposes was not feasible in these cases. For these reasons, the current geostationary satellites do not appear to be capable of estimating mesoscale rainfall in mid-latitude rain areas characterized by relatively shallow convection even though the IR sensors are able to distinguish very broad rainfall areas from nearby areas with little or no rain.

6. CONCLUSIONS

Radar studies of mid-latitude cyclones have shown that precipitation is typically organized into rainbands that have clearly definable characteristics and behavior.⁹ Austin and Houze⁸ showed that the rainbands can frequently be characterized by areas referred to as small mesoscale areas (SMSAs), large mesoscale areas (LMSAs), and cells. This study focused on cases of mid-latitude precipitation not associated with deep convection. The analysis was extended to visible and infrared (IR) imagery from geostationary satellites that provide fresh images on a half-hourly cycle. Three 1978 storm situations were selected for study: Two of them, 19 April and 15 May, had substantial echo areas conducive to extensive study; the third, 5 May, was characterized by small scattered echoes, none of which met the criteria for SMSAs or LMSAs.

Table 11. Correlation Coefficients of the Time Variation of Both Radar Echo Area and Precipitation Mass Flux to Satellite IR Area for the Major Echoes

Echo A			Echo B		
Satellite Digital Count	Correlation Coefficient		Satellite Digital Count	Correlation Coefficient	
	Area	Rain Mass Flux		Area	Rain Mass Flux
185	-0.31	-0.30	175	0.24	0.32
186	-0.52	-0.55	176	0.35	0.42
187	-0.55	-0.56	177	0.30	0.27
188	-0.42	-0.35	178	0.60	0.68
189	0.11	0.14	179	0.24	0.26
190	0.56	0.54	180	0.21	0.19
191	0.25	0.32	181	0.20	0.15
192	0.15	0.21	182	0.10	0.17
193	0.11	0.18	183	0.19	0.26
194	0.06	0.09			

Echo C			Echo D		
Satellite Digital Count	Correlation Coefficient		Satellite Digital Count	Correlation Coefficient	
	Area	Rain Mass Flux		Area	Rain Mass Flux
180	-0.36	-0.39	193	-0.43	-0.38
181	-0.40	-0.42	194	-0.48	-0.42
182	-0.27	-0.29	195	-0.21	-0.18
183	0.29	0.32	196	-0.15	0.09
184	0.37	0.40	197	0.13	0.21
185	0.49	0.49	198	0.19	0.25
186	0.49	0.50	199	0.20	0.28
187	0.40	0.37	200	0.03	0.09
188	0.09	0.15			

Echo E		
Satellite Digital Count	Correlation Coefficient	
	Area	Rain Mass Flux
172	0.07	0.13
173	0.06	0.14
174	0.12	0.12
175	-0.08	-0.10
176	-0.07	-0.09
177	0.11	0.17
178	0.29	0.27

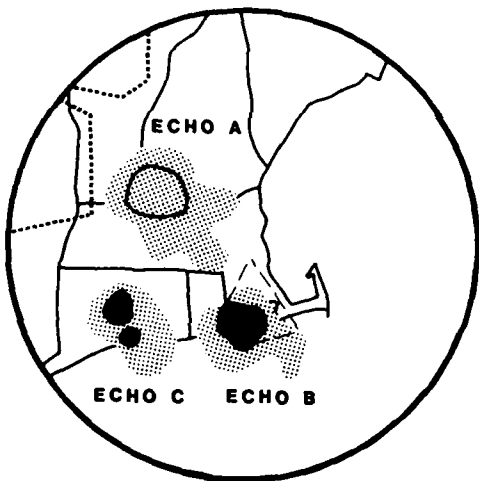


Figure 16. The 1902 GMT, 26-dBZ (stippled areas), 30-dBZ (dark areas) Radar Reflectivity Levels and the 1900 GMT Colder IR Areas Associated With Major Echo A (short dashed lines), B (long dashed line) and C for 19 April 1978. The short dashed lines within and to the west and northwest of echo A represent the 192 IR digital level while the long dashed line near echo B represents the 181 IR digital level. Note that the heaviest areas of precipitation and coldest IR regions are not precisely in the same location. There was no evidence in the 1900 GMT image that echo C was present. There was also no evidence of precipitation to the west and northwest of echo A in the 1902 GMT radar map

Analyses of the two rainband cases showed that the major echoes and LMSAs contained within them have lifetimes that are long relative to the satellite sensing time scale. In addition, about half the SMSAs and all cells that were detected by radar within the major echoes, for these two cases, had durations of about one-half hour. It is important to note, however, that the typical lifetime of SMSAs observed in this study is at the lower end of a time scale first proposed by Austin and Houze.⁸

The size of mesoscale areas within the rainbands, together with the total contribution of these mesoscale areas to rainfall amounts over large areas, was found to be an important factor in determining the ultimate potential of satellite rainfall estimation. Major echoes, LMSAs, and SMSAs typically are large enough in area for detection by current geostationary satellite sensors. Radar rainfall mass-flux estimates for the cases examined in this study show that when

a single average rainfall estimate based on satellite imagery is desired for a large area (for example 10,000 km²) and for a period of several hours, then major echoes, LMSAs, and SMSAs must be detected and monitored by the satellite. In this study, which dealt with cases of mid-latitude precipitation with shallow convection, radar mass-flux estimates of rainfall for cells contributed just 6 percent to rainfall averages over large areas. As such the contribution from cells could be ignored with relatively little loss of accuracy. However, in many other situations with deep convective cells, their contribution to total area rainfall is significant (as much as 95 percent of rainfall in flash-flood situations or over tropical oceans is accounted for by convective cells) and cannot be ignored. On the other hand, it was found that SMSAs need to be detected and monitored because they can make a substantial contribution. On 19 April, SMSAs contributed about 14 percent to the total mass rainfall flux of major echoes, while the SMSAs on 15 May contributed over a third of the mass rainfall flux of the major echo that contained them. The radar analyses of the rainbands examined in this study indicate that the spatial and temporal resolution of the current geostationary satellites are adequate for estimating rainfall amounts contributed by LMSAs, major echoes, and most SMSAs. The problem, therefore, was to determine whether or not the GOES satellite could detect these mesoscale rain areas.

Visual inspection of the satellite imagery indicated that stratiform clouds prevailed in all three cases. However, comparison of enhanced IR images with rain gages records showed that areas below an IR threshold had relatively little rain. Also the precipitating cloud areas for two of the cases (19 April and 15 May) had slightly colder IR temperatures relative to nearby nonprecipitating clouds. Thus, the finding that the relatively colder regions in the IR imagery could separate large areas with little or no rain from smaller areas with rain is encouraging. Comparison of the hourly rain gage data and IR imagery showed that most of the rain gage locations that reported measurable rain were within or in the immediate vicinity of a subjectively determined threshold area. However, within the IR threshold region, the satellite sensors could not readily distinguish rain gage sites that reported measurable rain from those that did not. Approximately 75 percent of the rain gages within the IR threshold region reported no measurable rainfall. On a broader scale, comparison of the radar echo rainbands in two of the cases in this study with the IR threshold area showed some agreement in terms of general shape and orientation. However, the visible imagery showed no ability to differentiate between precipitating and nonprecipitating clouds.

This study examined the relationship between satellite-observed quantities, radar and rain gage data over large mesoscale areas for the purpose of establishing a basis for estimating an average rainfall amount for synoptic scale systems from satellite imagery. In this regard, it was necessary to determine whether a

threshold of IR temperature could be defined (calibrated) with radar or rain gage data. This IR threshold region could then be used to estimate an average rain amount over large cold cloud areas. Hourly rain gage data and associated radar and satellite data were analyzed for two cases, 19 April and 15 May 1978. The 24-hour rainfall totals for the two days were essentially the same. Rain was more organized and widespread with slightly larger rainfall rates on 19 April than on 15 May. The subjectively determined IR threshold used to delineate raining clouds was found to be different for the two cases, being slightly colder on 15 May. A comparison of the time change of radar echo area and mass flux estimates of rain to the time change of IR areas over the major echoes, showed little correspondence. On the average, correlation coefficients for the time change of both radar echo area and mass flux of rain to the time variation of IR satellite areas were 0.06 and 0.10, respectively. Inspection of the IR imagery revealed that the location of the coldest areas over the major echoes did not always coincide with the heaviest radar determined rain areas. Thus, on the basis of the cases examined in this study, there is no immediately obvious useful relationship between IR satellite imagery and rainfall amounts. This conclusion applies only to mid-latitude situations characterized by mesoscale rainbands with relatively shallow convection.

References

1. Stout, J. E., and Martin, D. W. (1979) Estimating GATE rainfall with geosynchronous satellite images, Mon. Wea. Rev. 107:585-598.
2. Griffith, C. G., Augustine, J. A., Woodley, W. J., and Meiten, J. G. (1980) The estimation of convective rainfall from thermal infrared, geosynchronous satellite data (to be published).
3. Houze, R. A., Jr., and Cheng, C. P. (1977) Radar characteristics of tropical convection observed during GATE: Mean properties and trends over the summer season, Mon. Wea. Rev. 105:964-980.
4. Scofield, R. A., and Oliver, V. J. (1977) A scheme for estimating convective rainfall from satellite imagery, NOAA Tech. Memo. NESS 86, Washington, D.C., 47 pp.
5. Woodley, W. L., Griffith, C. G., Griffin, J. S., and Stromatt, S. C. (1980) The inference of GATE convective rainfall from SMS-1 imagery, J. Appl. Meteorol. 19:388-408.
6. Lovejoy, S., and Austin, G. L. (1979) The delineation of rain areas from visible and IR satellite data for GATE and midlatitudes, Atmos.-Oceans 20:79-82.
7. Wylie, D. P. (1979) An application of a geostationary satellite rain estimation technique to an extratropical area, J. Appl. Meteorol. 18:1640-1648.
8. Austin, P. M., and Houze, R. A., Jr. (1972) Analysis of the structure of precipitation patterns in New England, J. Appl. Meteorol. 11:926-935.
9. Harrold, T. W., and Austin, P. M. (1979) The structure of precipitation systems - A review, J. de Rech. Atmos. 8:41-57.
10. Reed, R. W. (1972) Characteristics and Development of Mesoscale Precipitation Area in Extra-tropical Cyclones, SM Thesis, Dept. of Meteorology, M.I.T., Cambridge, Massachusetts, 94 pp.
11. Bjerkaas, C. L. (1977) Mesoscale Characteristics of Precipitation in a Disturbance of the Tropical Eastern Atlantic, SM Thesis, Dept. of Meteorology, M.I.T., Cambridge, Mass., 104 pp.

12. Austin, P. M. (1978) Characteristics of rain echoes defined by a threshold intensity, 18th Conference on Radar Meteorology, Amer. Meteor. Soc., Boston, Massachusetts, 165-170.
13. Freeman, L. E. (1976) Sizes and Intensities of Mesoscale Precipitation Areas as Depicted by Digital Radar Data, SM Thesis, Dept. of Meteorology, M.I.T., Cambridge, Massachusetts, 96 pp.
14. Personal correspondence with Spiros G. Geotis of the M.I.T. Weather Radar Office.
15. Muench, H. S., and Keegan, T. J. (1979) Development of Techniques to Specify Cloudiness and Rainfall Rate Using GOES Imagery Data, AFGL-TR-79-0255, AD A084 755, Bedford, Massachusetts, 46 pp.